THE JOURNAL OF PHYSICAL CHEMISTRY C

Article

Dimers and Trimers of Hollow Silicon Nanoparticles#: #Manipulating the Magnetic Hotspots

MirFaez Miri, and Mahdiyeh Sadrara

J. Phys. Chem. C, **Just Accepted Manuscript** • Publication Date (Web): 04 May 2017

ACS Publications

The Journal of Physical Chemistry C is published by the American Chemical Society. 1155 Sixteenth Street N.W., Washington, DC 20036

Dimers and Trimers of Hollow Silicon Nanoparticles: Manipulating the Magnetic Hotspots

MirFaez Miri*,† and Mahdiyeh Sadrara‡

†*Department of Physics, University of Tehran, P.O. Box 14395-547, Tehran, Iran*

‡*Department of Physics, Kharazmi University, P.O. Box 15719-14911, Tehran, Iran*

E-mail: mirfaez˙miri@ut.ac.ir

Abstract

We study magnetic and electric hotspots in the gaps of nanoparticle dimers and trimers composed of *hollow* silicon nanoparticles. We find that the hollow size markedly influences the overall shape of the field enhancement, in particular the peak magnitude and the peak position. The peak shifts about $100 - 200$ nm as the hollow size varies. Tuned magnetic hotspots allow one to better enhance the Raman optical activity and circular dichroism of molecules, the interaction of light and nanomagnets, etc..

Introduction

Metallic nanoparticles exhibit a plethora of interesting optical properties. Noteworthy, metallic nanoparticles supporting surface plasmons, may localize light in subwavelength volumes. Enhanced local electric fields enormously increase the interaction of light with quantum emitters such as atoms, molecules, and quantum dots. Plasmonic hot spots are promising for fluorescence enhancement,[1–4] surface enhanced Raman optical activity of chiral molecules,[5] surface enhanced Raman scattering,[6] second and third harmonic generation,[7,8] etc.. However, considerable ohmic losses at optical frequencies is a limitation for the performance of metallic nanoparticles.[9,10] For example, in the area of spectroscopic analysis of matter, the advantage of plasmonic field enhancement can be obstructed by a local temperature increase of order 50 K, which may affect the dielectric properties of the sample.[9] Recently, a lot of attention is being paid to dielectric nanoparticles with high permittivity, as an alternative to metallic nanoparticles. The optical properties of gallium arsenide (GaAs),[11] germanium (Ge),[12] gallium phosphide (GaP)[9] and silicon (Si) nanoparticles,[13–16] are thoroughly studied. Remarkably, Si dimer nanoantennas are shown to produce high surface enhanced fluorescence and surface enhanced Raman scattering, but with ultra-low heat conversion.[10] Metal-dielectric hybrid nanostructures are also promising. For example, efficient third harmonic generation from Si nanodisk-Au nanoring hybrid nanoantennas are shown.[17]

Experiments vividly demonstrate that high-index dielectric nanoparticles exhibit consid-

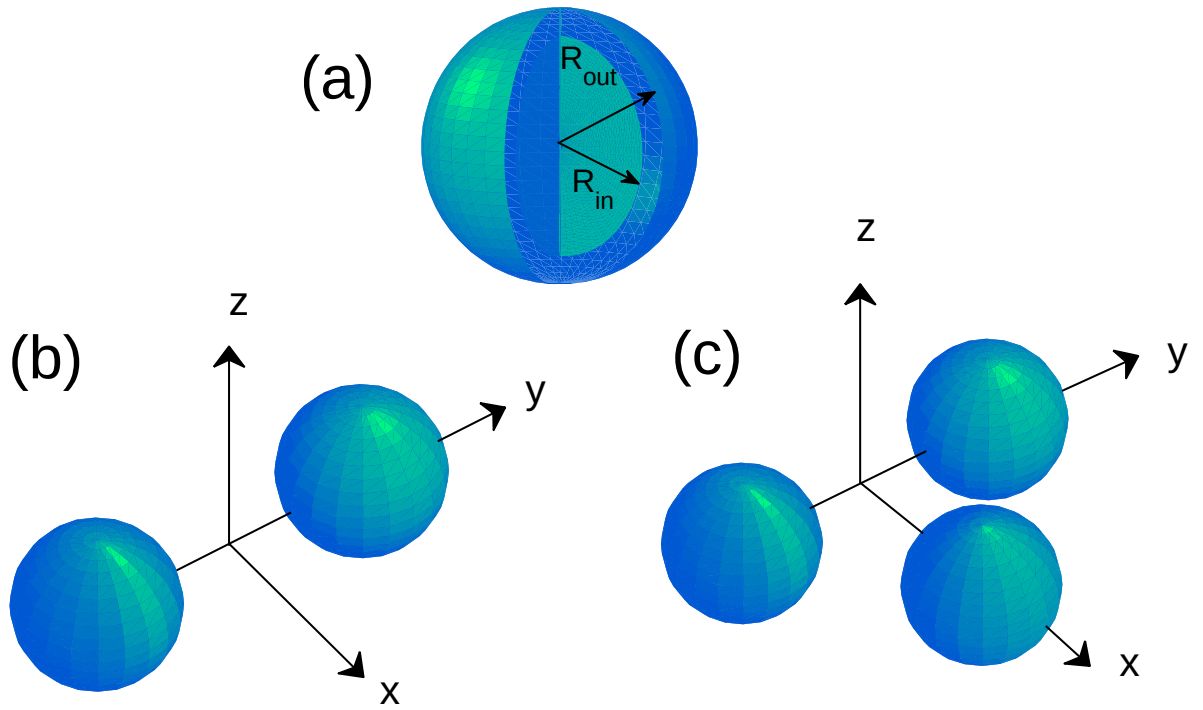

Figure 1: Schematic representation of (a) a single hollow particle, (b) a particle dimer, and (c) a particle trimer.

erable *magnetic* response in the visible frequency range.[13,14] The Mie theory reveals that both electric and magnetic modes of a dielectric spherical particle can be excited.[18] This can be understood intuitively: The circular displacement currents driven by an incident electric field, induce a magnetic dipole moment in the particle. The magnetic response offers a wide range of applications including broadband omnidirectional antireflection coating,[19] polarization-independent metadevice for optical wavefront control,[20] spectrally selective chiral metasurfaces,[21] superdirective dielectric nanoantennas,[22] and switchable directional scattering of light.[23,24]

Strong magnetic field intensities in subwavelength gaps separating dielectric particles are theoretically predicted[15] and experimentally observed.[25,26] *Magnetic hotspots* deserve special attention. Indeed the Hamiltonian

$$H_{int} = -\mathbf{d} \cdot \mathbf{E} - \mathbf{m} \cdot \mathbf{B} + \ldots \quad (1)$$

describes the salient features of the interaction between a quantum emitter and an electromagnetic field, where $\mathbf{d}$ and $\mathbf{m}$ are the electric and magnetic dipole moment of the emitter. Thus we expect magnetic hotspots to offer a route to enhance: (i) Magnetic-dipole transitions of lanthanide ions such as trivalent europium (Eu^{3+}), terbium (Tb^{3+}), and erbium (Er^{3+}),[27] in view of applications in rare-earth-doped fiber lasers and amplifiers. Note that conventional plane waves do not strongly excite electric-dipole forbidden transitions of atoms and molecules. (ii) Circular dichroism, the property of differential absorption of right- and left-circularly polarized light. Note that $\mathrm{Im}(\mathbf{d}\cdot\mathbf{m}) \neq 0$ is a prerequisite for exhibiting circular dichroism.[28] Enhancing the sensitivity of circular dichroism spectroscopy, which is utilized to study conformations of biological molecules, helps to probe samples of low concentrations. (iii) Raman optical activity (ROA) of molecules, i.e. the difference in the Raman scattered intensities in right- and left-circularly polarized incident light. ROA spectra provides invaluable information on tertiary folding, secondary structure and the orientation of individual residues in proteins and nucleic acids.[5] When the molecule resides in the hotspot of a Si dimer, the signal can be about 60 times larger.[29] (iv) Surface enhanced fluorescence and surface enhanced Raman scattering. Si dimer nanoantennas enhance the signal by a factor about 1000.[10] (v) Interaction between a nanomagnet (small ferromagnet) and light. Large quantum-coherent magnet-photon coupling, in excess of several THz, is of importance in quantum information processing.[30,31]

To date, most researches on the magnetic hotspots have been focused on the magnitude of the field enhancement. However, the necessity to the field enhancement at a wavelength corresponding to transition between electronic levels of the quantum emitter, is not well emphasized. Here we propose to use *hollow* dielectric nanoparticles to control the wavelength dependence of the enhancement factor. Incidentally, the facile preparation of silicon hollow spheres are reported.[32,33]

The effect of the hollow size on the optical response of a cluster of nanoparticles can be understood heuristically: Each small particle can be modelled as a pair of an electric

dipole and a magnetic dipole. To treat the interaction of light and cluster, one considers the local field acting on any dipole as a superposition of the incident field and secondary fields produced by other dipoles. The local electric (magnetic) field and the electric polarizability (magnetic polarizability) determine the electric (magnetic) dipole induced in the particle. This leads to a set of coupled electric and magnetic dipole equations (CEMD),[34] whose solution determines the electromagnetic field distribution. Both electric and magnetic polarizabilities depend on the inner radius R_{in} and outer radius R_{out} of the hollow particle. Thus now it is apparent that the field enhancement factor of a cluster depends on the hollow size of its constituent particles. However, the dipole approximation fails when the particles are too near to each other and the enhancement factor is expectedly large. To go beyond CEMD, one can use finite-difference time-domain (FDTD) or finite element method (FEM) to perform electromagnetic simulations. These calculations are too computationally demanding. Thus, here we employ an extension of the Mie theory to calculate electromagnetic fields inside a cluster of spherical particles, in a reasonable computational time (a few hours). We reproduced some results of Ref.[15] as a test of our code.

Here we study magnetic and electric hotspots in the gaps of nanoparticle dimer and nanoparticle trimer shown in Figure 1. We compare the field enhancing performance of clusters, one composed of hollow silicon nanoparticles, and the other composed of hollow silver nanoparticles. We show that the hollow size $f = (R_{in}/R_{out})^3$ can be invoked to tailor both the magnitude and the position of the maximum field enhancement. Using silicon particles of outer radius 120 nm and hollow size 0.4 at a gap distance of 10 nm, magnetic field enhancement as large as 10.48 is achievable. Silver particles of outer radius 80 nm and hollow size 0.8 at a gap distance of 10 nm, provide electric field enhancement as large as 50.38. Quite remarkably, for 80 and 120 nm radius Si particles, the shift of pronounced peak per hollow size variation, can reach 250 nm. In other words, the maxima of magnetic and electric field enhancements shift about $100-200$ nm as one varies the hollow size in the range of $0-0.8$. This wavelength tuning of magnetic and electric hotspots allows one to better

enhance the Raman optical activity of molecules, the interaction of light and nanomagnets, etc..

Theory

Multipole expansion of the electromagnetic field

We characterize the αth core-shell nanoparticle by its position $\mathbf{R}_\alpha$, inner radius R_{in}, outer radius R_{out}, core refractive index n_1, and shell refractive index n_2. We use

$$f = (\frac{R_{in}}{R_{out}})^3 \tag{2}$$

to represent the ratio of the core volume to the total volume of the nanoparticle. We assume that all the electromagnetic fields depend on time through $e^{-i\omega t}$. We define $k_v = \frac{\omega}{c}$ and $k = nk_v$, where c is the velocity of light in vacuum and n is the refractive index of the host medium. We use $\hat{\mathbf{k}}_I$ and $\hat{\mathbf{u}}_{I\eta}$ $(\eta = 1, 2)$ to denote the wave vector and polarization vector of the incident plane wave, respectively. We use $\hat{\mathbf{k}}_S$ and $\hat{\mathbf{u}}_{S\eta}$ $(\eta = 1, 2)$ to describe the scattered field. We denote an incident (scattered) field polarized along $\hat{\mathbf{u}}_{I\eta}$ ($\hat{\mathbf{u}}_{S\eta}$) by $\mathbf{E}_{I\eta}$ ($\mathbf{E}_{S\eta}$). We use cgs units.

The vector multipole fields are solutions of the Maxwell equations that are simultaneous eigenvectors of the angular momentum operators $\mathbf{L^2}$ and L_z .[35]

$$\begin{aligned}
\mathbf{J}^{(1)}_{lm}(\mathbf{r}, k) &= j_l(kr)\mathbf{X}_{lm}(\hat{\mathbf{r}}), \\
\mathbf{J}^{(2)}_{lm}(\mathbf{r}, k) &= \frac{1}{k}\nabla \times \mathbf{J}^{(1)}_{lm}(\mathbf{r}, k), \\
\mathbf{H}^{(1)}_{lm}(\mathbf{r}, k) &= h_l(kr)\mathbf{X}_{lm}(\hat{\mathbf{r}}), \\
\mathbf{H}^{(2)}_{lm}(\mathbf{r}, k) &= \frac{1}{k}\nabla \times \mathbf{H}^{(1)}_{lm}(\mathbf{r}, k),
\end{aligned} \tag{3}$$

where j_l and h_l are celebrated spherical Bessel function and spherical Hankel function of the

first kind, respectively. In Eq. (3), the vector function $\mathbf{X}_{lm} = [l(l+1)]^{-1/2}\mathbf{L}Y_{lm}$, where the spherical harmonic Y_{lm} is the simultaneous eigenfunction of $\mathbf{L^2}$ and L_z. It is also convenient to introduce transverse vector harmonics

$$\begin{aligned} \mathbf{Z}^{(1)}_{lm}(\hat{\mathbf{k}}) &= \mathbf{X}_{lm}(\hat{\mathbf{k}}), \\ \mathbf{Z}^{(2)}_{lm}(\hat{\mathbf{k}}) &= \mathbf{X}_{lm}(\hat{\mathbf{k}}) \times \hat{\mathbf{k}}. \end{aligned} \tag{4}$$

The incident field $\mathbf{E}_{I\eta} = E_0\hat{\mathbf{u}}_{I\eta}e^{i\mathbf{k}\cdot\mathbf{r}}$, the scattered field $\mathbf{E}_{S\eta}$, the field in the core of the αth particle $\mathbf{E}_{TC\eta\alpha}$, and the field in the shell of the αth particle $\mathbf{E}_{TS\eta\alpha}$ are expanded as

$$\begin{aligned} \mathbf{E}_{I\eta}(\mathbf{r}) &= E_0 \sum_{plm} W^{(p)}_{I\eta lm}\ \mathbf{J}^{(p)}_{lm}(\mathbf{r}, k), \\ \mathbf{E}_{S\eta}(\mathbf{r}) &= E_0 \sum_{\alpha} \sum_{plm} \mathcal{A}^{(p)}_{\eta\alpha lm}\ \mathbf{H}^{(p)}_{lm}(\mathbf{r}_\alpha, k), \\ \mathbf{E}_{TC\eta\alpha}(\mathbf{r}) &= E_0 \sum_{plm} \mathcal{C}^{(p)}_{\eta\alpha lm}\ \mathbf{J}^{(p)}_{lm}(\mathbf{r}_\alpha, k_1), \\ \mathbf{E}_{TS\eta\alpha}(\mathbf{r}) &= E_0 \sum_{plm} \left(\mathcal{S}^{(p)}_{\eta\alpha lm}\ \mathbf{J}^{(p)}_{lm}(\mathbf{r}_\alpha, k_2) + \mathcal{V}^{(p)}_{\eta\alpha lm}\ \mathbf{H}^{(p)}_{lm}(\mathbf{r}_\alpha, k_2)\right), \end{aligned} \tag{5}$$

where $\mathbf{r}_\alpha = \mathbf{r} - \mathbf{R}_\alpha$, $p = 1, 2$, $k_1 = n_1 k_v$, and $k_2 = n_2 k_v$. Indeed $W^{(p)}_{I\eta lm} \equiv W^{(p)}_{lm}(\hat{\mathbf{u}}_{I\eta}, \hat{\mathbf{k}}_I) = 4\pi i^{p+l-1}\hat{\mathbf{u}}_{I\eta} \cdot \mathbf{Z}^{(p)^\star}_{lm}(\hat{\mathbf{k}}_I)$.

Note that in Eq. (5) the incident field is a sum of multipole fields centered at $\mathbf{R}_0 = 0$, but the scattered field is a sum of multipole fields with different origins. Upon using the addition theorem, whole fields can be expressed in terms of multipole fields with a certain origin $\mathbf{R}_\alpha$.

$$\begin{aligned} \mathbf{E}_{S\eta} &= E_0 \sum_{plm} \Big[\mathcal{A}^{(p)}_{\eta\alpha lm}\ \mathbf{H}^{(p)}_{lm}(\mathbf{r}_\alpha, k) \\ &\quad + \sum_{\alpha' p' l' m'} \mathcal{H}^{(pp')}_{\alpha lm\alpha' l' m'} \mathcal{A}^{(p')}_{\eta\alpha' l' m'}\ \mathbf{J}^{(p)}_{lm}(\mathbf{r}_\alpha, k)\Big], \end{aligned} \tag{6}$$

$$\mathbf{E}_{I\eta} = E_0 \sum_{plm} \sum_{p' l' m'} \mathcal{J}^{(pp')}_{\alpha lm 0 l' m'} W^{(p')}_{I\eta l' m'}\ \mathbf{J}^{(p)}_{lm}(\mathbf{r}_\alpha, k), \tag{7}$$

where $\mathcal{H}^{(pp')}_{\alpha lm\alpha' l'm'}$ and $\mathcal{J}^{(pp')}_{\alpha lm0l'm'}$ are given in Ref.[35] Now one must impose the boundary conditions across the inner and outer surfaces of αth particle. Eliminating the amplitudes of the internal fields $\mathcal{C}^{(p)}_{\eta\alpha lm}$, $\mathcal{S}^{(p)}_{\eta\alpha lm}$ and $\mathcal{V}^{(p)}_{\eta\alpha lm}$, one finds a set of linear algebraic equations for the amplitudes of the scattered fields $\mathcal{A}^{(p)}_{\eta\alpha lm}$:

$$\sum_{\alpha'}\sum_{p'l'm'}\mathcal{M}^{(pp')}_{\alpha lm\alpha' l'm'}\mathcal{A}^{(p')}_{\eta\alpha' l'm'} = -\mathcal{W}^{(p)}_{I\eta\alpha lm}. \tag{8}$$

Note that $\mathcal{W}^{(p)}_{I\eta\alpha lm} = \sum_{p'l'm'}\mathcal{J}^{(pp')}_{\alpha lm0l'm'}W^{(p)}_{I\eta l'm'}$ is written in terms of the known amplitudes of the incident field. Moreover

$$\mathcal{M}^{(pp')}_{\alpha lm\alpha' l'm'} = (R^{(p)}_{\alpha l})^{-1}\delta_{\alpha\alpha'}\delta_{pp'}\delta_{ll'}\delta_{mm'} + \mathcal{H}^{(pp')}_{\alpha lm\alpha' l'm'}, \tag{9}$$

where $R^{(p)}_{\alpha l}$ are the Mie coefficients for the scattering from the αth core-shell particle.

The task is now to calculate the Mie coefficients. We recall that

$$\hat{\mathbf{r}}\times(\mathbf{E}_{TC}-\mathbf{E}_{TS}) = 0, \tag{10}$$

$$\hat{\mathbf{r}}\times(\mathbf{H}_{TC}-\mathbf{H}_{TS}) = 0, \tag{11}$$

and

$$\hat{\mathbf{r}}\times(\mathbf{E}_{I}+\mathbf{E}_{S}-\mathbf{E}_{TS}) = 0, \tag{12}$$

$$\hat{\mathbf{r}}\times(\mathbf{H}_{I}+\mathbf{H}_{S}-\mathbf{H}_{TS}) = 0, \tag{13}$$

are the boundary conditions across the inner and outer surfaces of a core-shell particle, respectively. It is more convenient to project the fields along the transverse vector harmonics and rewrite the boundary conditions. For example, the boundary condition (10) can be rephrased as $\int \mathbf{E}_{TC\eta}\cdot\mathbf{Z}^{(p)*}_{lm}d\Omega = \int \mathbf{E}_{TS\eta}\cdot\mathbf{Z}^{(p)*}_{lm}d\Omega$. Now using the the identity $\int \mathbf{Z}^{(p')}_{l'm'}\cdot\mathbf{Z}^{(p)*}_{lm}d\Omega = \delta_{pp'}\delta_{ll'}\delta_{mm'}$ allows one to access a set of linear algebraic equations for $\mathcal{C}^{(p)}_{\eta lm}$, $\mathcal{S}^{(p)}_{\eta lm}$, and $\mathcal{V}^{(p)}_{\eta lm}$

whose solution yields the Mie coefficients

$$R_l^{(1)}=\frac{m_2u_l(y)[u_l'(m_2y)-B_l\chi_l'(m_2y)]-u_l'(y)[u_l(m_2y)-B_l\chi_l(m_2y)]}{m_2\omega_l(y)[u_l'(m_2y)-B_l\chi_l'(m_2y)]-\omega_l'(y)[u_l(m_2y)-B_l\chi_l(m_2y)]},$$
$$R_l^{(2)}=\frac{u_l(y)[u_l'(m_2y)-A_l\chi_l'(m_2y)]-m_2u_l'(y)[u_l(m_2y)-A_l\chi_l(m_2y)]}{\omega_l(y)[u_l'(m_2y)-A_l\chi_l'(m_2y)]-m_2\omega_l'(y)[u_l(m_2y)-B_l\chi_l(m_2y)]}. \quad (14)$$

Here the prime denotes the differentiation with respect to the argument, $h_l(z) = j_l(z)+iy_l(z)$, $u_l(z) = zj_l(z)$, $\chi_l(z) = -zy_l(z)$, $\omega_l(z) = zh_l(z)$, $x = kR_{in}$, $y = kR_{out}$, $m_1 = n_1/n$, $m_2 = n_2/n$, and

$$A_l = \frac{m_2u_l(m_2x)u_l'(m_1x) - m_1u_l'(m_2x)u_l(m_1x)}{m_2\chi_l(m_2x)u_l'(m_1x) - m_1\chi_l'(m_2x)u_l(m_1x)},$$
$$B_l = \frac{m_2u_l(m_1x)u_l'(m_2x) - m_1u_l(m_2x)u_l'(m_1x)}{m_2\chi_l'(m_2x)u_l(m_1x) - m_1u_l'(m_1x)\chi_l(m_2x)}. \quad (15)$$

We aim to calculate the electromagnetic field distribution in the vicinity of the particles. Indeed we expect the field enhancement to occur in the gaps between particles. We assume that the origin of the coordinate system is placed inside the cluster of particles. Since the multipole fields $\mathbf{J}_{lm}^{(1)}$ and $\mathbf{J}_{lm}^{(2)}$ are regular at the origin, the scattered near field can be expressed as

$$\mathbf{E}_{S\eta} = E_0 \sum_{plm} A_{\eta lm}^{(p)}\ \mathbf{J}_{lm}^{(p)}(\mathbf{r}, k). \quad (16)$$

According to the Maxwell equation $\nabla \times \mathbf{E}_S = \frac{i\omega}{c}\mathbf{B}_S$, and the identities $\mathbf{J}_{lm}^{(1)}(\mathbf{r}, k) = \frac{1}{k}\nabla \times \mathbf{J}_{lm}^{(2)}(\mathbf{r}, k)$ and $\mathbf{J}_{lm}^{(2)}(\mathbf{r}, k) = \frac{1}{k}\nabla \times \mathbf{J}_{lm}^{(1)}(\mathbf{r}, k)$, the magnetic field is

$$\mathbf{B}_{S\eta} = -inE_0 \sum_{plm} A_{\eta lm}^{(p')}\ \mathbf{J}_{lm}^{(p)}(\mathbf{r}, k) \quad (p \neq p'). \quad (17)$$

Comparing Eqs. (5) and (16) leads to the key result

$$A_{\eta lm}^{(p)} = \sum_{\alpha'} \sum_{p'l'm'} \mathcal{H}_{0lm\alpha'l'm'}^{(pp')} \mathcal{A}_{\eta\alpha'l'm'}^{(p')}, \tag{18}$$

which states that the solution of linear algebraic equations (8) can be straightforwardly used to obtain the near fields $\mathbf{E}_S$ and $\mathbf{B}_S$. The following expressions for the vector multipole fields greatly facilitate the calculation of electromagnetic fields:

$$\begin{aligned}
&\mathbf{J}_{lm}^{(1)}(\mathbf{r},k) = \\
&\Big\{(mY_{lm}\cos\theta + s_l^m Y_{l,m+1}\sin\theta e^{-i\phi} + s_l^{-m} Y_{l,m-1}\sin\theta e^{i\phi})\hat{r} \\
&-(mY_{lm}\sin\theta - s_l^m Y_{l,m+1}\cos\theta e^{-i\phi} - s_l^{-m} Y_{l,m-1}\cos\theta e^{i\phi})\hat{\theta} \\
&-i(s_l^m Y_{l,m+1} e^{-i\phi} - s_l^{-m} Y_{l,m-1} e^{i\phi})\hat{\phi}\Big\}\frac{j_l(kr)}{\sqrt{l(l+1)}}, \\
&\mathbf{J}_{lm}^{(2)}(\mathbf{r},k) = \frac{i}{kr}\sqrt{l(l+1)}j_l(kr)Y_{lm}\hat{r} \\
&+\frac{[krj_l(kr)]'}{kr\sqrt{l(l+1)}}\Big\{i(s_l^m Y_{l,m+1} e^{-i\phi} - s_l^{-m} Y_{l,m-1} e^{i\phi})\hat{\theta} \\
&-(mY_{lm}\sin\theta - s_l^m Y_{l,m+1}\cos\theta e^{-i\phi} - s_l^{-m} Y_{l,m-1}\cos\theta e^{i\phi})\hat{\phi}\Big\}.
\end{aligned} \tag{19}$$

Here $s_l^m = \frac{1}{2}\sqrt{(l-m)(l+m+1)}$, and (r,θ,ϕ) denote the spherical coordinates of point $\mathbf{r}$.

A few remarks are in order. i) The $\mathbf{H}_{lm}^{(p)}(\mathbf{r},k)$ multipole fields satisfy the radiation condition at the infinity. Thus in the *far zone*, one expands the scattered fields in terms of $\mathbf{H}_{lm}^{(p)}(\mathbf{r},k)$ rather than $\mathbf{J}_{lm}^{(p)}(\mathbf{r},k)$.[35] ii) Here we assume that all particles are similar, but this assumption can be relaxed straightforwardly. iii) Practically, the set of linear equations (8) must be truncated to some finite order. Committed to the numerical stability of the results, one performs multipole expansions of the fields up to a multipole order $l_{\max}$. We use $l_{\max} \geqslant 11$.

Dielectric functions of silicon and silver

We obtain the optical constants of silicon from Green and Keevers.[36] For the the optical constants of bulk silver, we use the analytic model of Rioux *et al.*[37] which well reproduces the experimental data of Johnson and Christy.[38] To consider the finite size effects in silver nanoparticles, we use the following dielectric function:[39]

$$\varepsilon(\omega) = \varepsilon^{\rm bulk}(\omega) + \frac{\omega_p^2}{\omega^2 + {\rm i}\gamma_{\rm bulk}\omega} - \frac{\omega_p^2}{\omega^2 + {\rm i}\gamma\omega}. \quad (20)$$

Here ω_p is the plasma frequency, $\gamma = \gamma_{\rm bulk} + v_{\rm F}/R_{eff}$ is the radius-dependent relaxation, $v_{\rm F}$ is the Fermi velocity, and

$$R_{eff} = \frac{4(R_{out}^3 - R_{in}^3)}{3(R_{out}^2 + R_{in}^2)} \quad (21)$$

is the effective radius.[40] For silver, $\omega_p = 1.300 \times 10^{16}$ s^{-1}, $\gamma_{\rm bulk} = 3.409 \times 10^{13}$ s^{-1}, and $v_{\rm F} = 1.4 \times 10^8$ cm/s. We assume that the refractive index of the host medium is $n = 1$.

Results

We study Si particles of outer radius 40, 80 and 120 nm. The extinction spectrum of a solid Si particle of radius 40 nm exhibits a magnetic dipole resonance at wavelength $\lambda = 2\pi/k_v = 420$ nm. A solid Si particle of radius 80 nm has an electric dipole resonance at 518 nm and a magnetic dipole resonance at 642 nm. Increasing the radius to 120 nm, a magnetic quadrapole resonance at 660 nm, an electric dipole resonance at 700 nm, and a magnetic dipole resonance at 905 nm appear. We thus expect small clusters composed of such Si particles to exhibit interesting properties in the window $400 < \lambda < 1000$ nm.

Magnetic and electric hotspots in nanoparticle dimers

We assume that two similar particles are at positions $\mathbf{r}_1 = (0, R_{out} + d_p/2, h_p)$ and $\mathbf{r}_2 = (0, -R_{out} - d_p/2, h_p)$. We study the field enhancement factors $|H/H_0|$ and $|E/E_0|$, where

H and E denote the amplitudes of the total magnetic and electric fields at the observation point. Here we assume the gap $d_p = 10$ nm and $h_p = 1$ nm.

Figure 2 shows the enhancement factors of Si and Ag dimers. Here $\mathbf{E}_I \| \hat{\mathbf{x}}$, i.e. the incident electric field is perpendicular to the dimer axis, $\mathbf{k}_I = -k\hat{\mathbf{z}}$, and the fields are calculated at the dimer center $(\mathbf{r}_1 + \mathbf{r}_2)/2$. Quite remarkably, $|H/H_0|$ as large as $(7.22, 8.7, 10.48)$ is achievable with Si particles of outer radius $(40, 80, 120)$ nm, while using Ag particles, $|H/H_0|$ is always less than 1. Moreover, one obtains $|H/H_0| \sim 10.48$ using hollow Si particles of $f = 0.4$, but not using solid Si particles. Using 40 nm radius Si particles, $|H/H_0|$ exhibits one peak. With larger 80 and 120 nm radius Si particles, $|H/H_0|$ has *two* pronounced peaks. Figure 2 vividly shows that the strong peaks of $|H/H_0|$ shift considerably as the hollow size of Si particle varies. For example, the strongest peak $\sim (8.52, 10.41, 10.48, 5.89, 3.17)$ occurs at the wavelength $(950, 660, 612, 560, 580)$ nm, when $f = (0, 0.2, 0.4, 0.6, 0.8)$ and $R_{out} = 120$ nm. Placed at the wavelength $(680, 900, 820, 720, 420)$ nm, the second peak $\sim (8.0, 7.62, 6.32, 4.81, 2.55)$ is also of use. Note that to obtain the largest possible $|H/H_0|$ at a certain wavelength, hollow particles maybe better than solid ones. For example, in the window $690 < \lambda < 830$ nm, hollow 120 nm radius Si particles of $f = 0.6$ are superior to their solid counterparts.

Quite interestingly, we find that the Si dimer may also enhance the electric field. Figure 2 demonstrates that $|E/E_0|$ as large as 4.28 is achievable with Si particles of $R_{out} = 120$ nm and $f = 0.2$, while using Ag particles of the same size, $|E/E_0|$ is less than 1.5. Decreasing the radius to $R_{out} = 80$ nm, then $|E/E_0|$ as large as 3.0 is reachable if one uses hollow Si particles of $f = 0.4$, rather than Ag particles. Further decreasing the radius to $R_{out} = 40$ nm, the highest electric field enhancement of the Si dimer is less than that of the Ag dimer. We observe that the strongest peak of $|E/E_0|$ shifts as the hollow size f varies. For example, as one varies the hollow size of 120 nm radius Si particles from 0.4 to 0.8, the maximum of $|E/E_0|$ shifts from 607 to 465 nm. In the case of Ag particles, the corresponding shift is from 375 to 490 nm. We observe again that to obtain the largest possible $|E/E_0|$ at a certain wavelength, hollow particles maybe better than solid ones. For example at the wavelength

800 nm, hollow Ag particles of $R_{out} = 120$ nm and $f = 0.8$ are preferable to their solid counterparts.

Figure 3 is same as Figure 2 except that here $\mathbf{E}_I \parallel \hat{\mathbf{y}}$, i.e. the incident electric field is parallel with the dimer axis. We find that the *polarization* of the incident field has a dramatic effect on the enhancement factors. Now Ag dimers provide the largest possible $|H/H_0|$: Solid Si particles and hollow Ag particles of $f = 0.2$, both of outer radius 120 nm, provide $|H/H_0|$ as large as 7.2 and 8.5, respectively. The position of the largest peak of $|H/H_0|$ depends on hollow size. For example, as one varies the hollow size of 120 nm radius Ag particles from 0.4 to 0.8, the peak shifts from 500 to 660 nm.

A comparison of Figures 2 and 3 immediately shows that the largest $|E/E_0|$ occurs when the incident electric field is parallel with the dimer axis. Expectedly, Ag dimers provide the largest possible $|E/E_0|$: For hollow 80 nm radius Ag particles of $f = 0.8$, $|E/E_0| \sim 50.38$ occurs at the wavelength 1020 nm. At other wavelengths $(420, 425, 445, 840)$ nm still impressive $|E/E_0| \sim (26.6, 27.2, 29.47, 35)$ can be obtained with Ag particles of the same radius and $f = (0, 0.2, 0.4, 0.6)$. Moreover, a reasonable $|E/E_0|$ can be guaranteed in a large window. For example, using 80 nm radius Ag particles of $f = 0.4$ or 120 nm radius Ag particles of $f = 0.8$ one finds $|E/E_0| > 20$ in windows $600 < \lambda < 1100$ nm and $660 < \lambda < 1100$ nm, respectively. Si particles can also be used for such purpose. For example, using solid 80 and 120 nm radius Si particles, $|E/E_0| > 10$ in broad windows $520 < \lambda < 1040$ nm and $700 < \lambda < 1100$ nm, respectively.

Magnetic and electric hotspots in nanoparticle trimers

Now we focus on the symmetric trimer shown in Figure 1. We assume that the particles positioned at $\mathbf{r}_1$, $\mathbf{r}_2$, and $\mathbf{r}_3 = (\sqrt{3}R_{out} + \sqrt{3}d_p/2, 0, h_p)$ are identical. As before we assume the gap $d_p = 10$ nm and $h_p = 1$ nm.

Figure 4 shows the enhancement factors of Si and Ag trimers. Here $\mathbf{E}_I \parallel \hat{\mathbf{x}}$, $\mathbf{k}_I = -k\hat{\mathbf{z}}$, and the fields are calculated at the midpoint $(\mathbf{r}_1 + \mathbf{r}_2)/2$. At first glance, Figures 2 and 4 are

not much different qualitatively. But a closer inspection reveals that the trimer allows one to further *fine tune* the wavelength of the maximum field enhancement. For example, now considerable $|H/H_0|$ occurs at the wavelength $(670, 640, 590, 530, 450)$ nm upon using 80 nm radius Si particles of hollow size $f = (0, 0.2, 0.4, 0.6, 0.8)$. Using similar 120 nm radius Si particles, the enhancement is maximum at $(960, 540, 840, 470, 415)$ nm.

The field enhancement at the centroid $(\mathbf{r}_1 + \mathbf{r}_2 + \mathbf{r}_3)/3$ is shown in Figure 5. Here $\mathbf{E}_I \parallel \hat{\mathbf{x}}$ or $\mathbf{E}_I \parallel \hat{\mathbf{y}}$, and $\mathbf{k}_I = -k\hat{\mathbf{z}}$. Figure 5 again clearly demonstrates that the hollow size f can be utilized to control the wavelength dependence of the field enhancement.

A few remarks are in order. (i) Nanoparticle dimers and trimers share a few properties, see Figure 6. For 40 nm radius Si particles, the peaks of $|H/H_0|$ and $|E/E_0|$ are around the wavelength 420 nm. But for 80 and 120 nm radius Si particles, the peaks are at higher wavelengths. (ii) For 40 nm radius Si particles, the peaks are almost independent of the hollow size f. But even for 40 nm radius Ag particles, the peak of $|E/E_0|$ well shifts as f varies. (iii) In the case of Si (Ag) clusters, the peaks blueshift (redshift) as f increases. (iv) $|H/H_0|$ and $|E/E_0|$ are nonmonotonic functions of the wavelength λ. However, in the case of 80 and 120 nm radius particles, the pronounced peaks of $|H/H_0|$ and $|E/E_0|$ shift almost monotonically as f varies. (v) The shift of pronounced peaks of $|H/H_0|$ and $|E/E_0|$ per hollow size variation, $|\Delta\lambda/\Delta f|$, can reach 250 nm. For example, Figure 6(a) shows $\Delta\lambda/\Delta f = -287$ when $R_{out} = 80$ nm and $\mathbf{E}_I \parallel \hat{\mathbf{x}}$, and Figure 6(b) shows $\Delta\lambda/\Delta f = -250$ when $R_{out} = 120$ nm and $\mathbf{E}_I \parallel \hat{\mathbf{y}}$. (vi) Concerning the maximum achievable enhancements, we find that the trimer has no overall advantage over the dimer, see Figures 2-5 (vii) The anisotropic dimer feels the polarization of the incident field when $\mathbf{k}_I = -k\hat{\mathbf{z}}$, see Figures 2 and 3. However, at the centroid of the symmetric trimer, the field enhancements are the same for both incident fields $\mathbf{E}_I \parallel \hat{\mathbf{x}}$ and $\mathbf{E}_I \parallel \hat{\mathbf{y}}$.

Are the fields larger at the center of symmetry of the cluster?

The points $(\mathbf{r}_1+\mathbf{r}_2)/2$ and $(\mathbf{r}_1+\mathbf{r}_2+\mathbf{r}_3)/3$ are the center of symmetry of the dimer and the equilateral trimer, respectively. At first, one may expect the maximum field enhancement to occur at such point. To exorcize this, Figure 7 presents $|H/H_0|$ and $|E/E_0|$ at a point displaced by the vector $\Delta h_p\hat{\mathbf{z}}$ from the center of symmetry at $\mathbf{r}_c$. Clearly, in many instances, the field reaches its maximum value when $\Delta h_p \neq 0$. This can be understood heuristically. The electric and magnetic polarizabilities, and hence the electric and magnetic dipoles induced in the particles, depend on the wavelength. Moreover, the dipoles induced in the particles depend on the polarization of the incident field. For a certain wavelength and polarization, the electromagnetic fields radiated by the dipoles *and* the incident field, may interfere more constructively at a point $\mathbf{r}_c+\Delta h_p\hat{\mathbf{z}}$ rather than at the point $\mathbf{r}_c$.

Summary and outlook

In summary, we have studied magnetic and electric hotspots in the gaps of nanoparticle dimers and trimers consisting of identical *hollow* silicon particles. We find that the hollow size $f=(R_{in}/R_{out})^3$ has a dramatic effect on the overall shape of the field enhancement factors $|H/H_0|$ and $|E/E_0|$, see Figures 2-5, and Figure 6 which summarizes some of our results. We find that the peak of field enhancement factor shifts considerably as the hollow size varies. Indeed for 80 and 120 nm radius Si particles, the shift of pronounced peaks of $|H/H_0|$ and $|E/E_0|$ per hollow size variation, $|\Delta\lambda/\Delta f|$, can reach 250 nm. Here we have considered nanoparticles at a large gap distance of 10 nm. However hollow silicon particles allow us to obtain significant magnetic field enhancement about 10.48.

A remark is in order. Experiments have resolved the electromagnetic mechanism of surface-enhanced light scattering at a single electric hot spot.[41] It is now known that to observe enhanced light scattering from a molecule, one needs an electric hot spot *and* a significant scattering cross section that allows the near field excitation of the molecule to

propagate via the nanoantenna to the far field region. We have pointed out that the magnetic hot spots may enhance Raman optical activity, circular dichroism, and fluorescence of molecules. Indeed the role of the scattering cross section of the molecule must not be forgotten.

Our work can be extended in several directions. GaAs, Ge, GaP and other dielectric nanoparticles can be studied straightforwardly. Here we have assumed that the cluster is composed of identical spherical particles. Particles of different outer radius, hollow size, and composition allow one to better tune the magnetic hotspot. The multipole expansion of the electromagnetic fields can be applied to aggregates containing many spheres. Inspired by the properties of two dimensional periodic array of clusters of plasmonic nanoparticles,[42] we are currently investigating metasurfaces composed of hollow dielectric nanoparticles.

References

(1) Ringler, M.; Schwemer, A.; Wunderlich, M.; Nichtl, A.; Kürzinger, K.; Klar, T. A.; Feldmann, J. Shaping emission spectra of fluorescent molecules with single plasmonic nanoresonators. *Phys. Rev. Lett.* **2008**, *100*, 203002.

(2) Gill, R.; Ru, E. C. Le. Fluorescence enhancement at hot-spots: the case of Ag nanoparticle aggregates. *Phys. Chem. Chem. Phys.* **2011**, *13*, 16366-16372.

(3) Bek, A.; Jansen, R.; Ringler, M.; Mayilo, S.; Klar, T.A.; Feldmann, J. Fluorescence enhancement in hot spots of AFM-designed gold nanoparticle sandwiches. *Nano Lett.* **2008**, *8*, 485-490.

(4) Punj, D.; Regmi, R.; Devilez, A.; Plauchu, R.; Moparthi, S. B.; Stout, B.; Bonod, N.; Rigneault, H.; Wenger, J. Self-assembled nanoparticle dimer antennas for plasmonic-enhanced single-molecule fluorescence detection at micromolar concentrations. *ACS Photonics* **2015**, *2*, 1099-1107.

(5) Abdali, S.; Blanch, E. W. Surface enhanced Raman optical activity (SEROA). *Chem. Soc. Rev.* **2008**, *37*, 980-992.

(6) Wei, H.; Xu, H. Hot spots in different metal nanostructures for plasmon-enhanced Raman spectroscopy. *Nanoscale* **2013**, *5*, 10794-10805.

(7) Thyagarajan, K.; Butet, J.; Martin, O. J. F. Augmenting second harmonic generation using Fano resonances in plasmonic systems. *Nano Lett.* **2013**, *13*, 1847-1851.

(8) Metzger, B.; Hentschel, M.; Schumacher, T.; Lippitz, M.; Ye. X.; Murray, C. B.; Knabe, B.; Buse, K.; Giessen, H. Doubling the efficiency of third harmonic generation by positioning ITO nanocrystals into the hot-spot of plasmonic gap-antennas. *Nano Lett.* **2014**, *14*, 2867-2872.

(9) Albella, P.; Alcaraz de la Osa, R.; Moreno, F.; Maier, S. A. Electric and magnetic field enhancement with ultralow heat radiation dielectric nanoantennas: considerations for surface-enhanced spectroscopies. *ACS Photonics* **2014**, *1*, 524-529.

(10) Caldarola, M.; Albella, P.; Cortés, E.; Rahmani, M.; Roschuk, T.; Grinblat, G.; Oulton, R. F.; Bragas. A. V.; Maier, S. M. Non-plasmonic nanoantennas for surface enhanced spectroscopies with ultra-low heat conversion. *Nat Commun.* **2015**, *6*, 7915.

(11) Person, S.; Jain, M.; Lapin, Z.; Sáenz, J. J.; Wicks, G.; Novotny, L. Demonstration of zero optical backscattering from single nanoparticles. *Nano Lett.* **2013**, *13*, 1806-1809.

(12) Gómez-Medina, R.; García-Cámara, B.; Suárez-Lacalle, I.; González, F.; Moreno, F.; Nieto-Vesperinas, M.; Sáenz, J. J. Electric and magnetic dipolar response of germanium nanospheres: interference effects, scattering anisotropy, and optical forces. *J. nanophoton.* **2011**, *5*, 053512-1-053512-9.

(13) Evlyukhin, A. B.; Novikov, S. M.; Zywietz, U.; Eriksen, R. L.; Reinhardt, C.; Bozhevol-

nyi, S. I.; Chichkov, B. N. Demonstration of magnetic dipole resonances of dielectric nanospheres in the visible region. *Nano Lett.* **2012**, *12*, 3749-3755.

(14) Permyakov, D.; Sinev, I.; Markovich, D.; Ginzburg, P.; Samusev, A.; Belov, P.; Valuckas, V.; Kuznetsov, A. I.; Luk'yanchuk, B. S.; Miroshnichenko, A. E.; Neshev, D. N.; Kivshar, Y. S. Probing magnetic and electric optical responses of silicon nanoparticles. *Appl. Phys. Lett.* **2015**, *106*, 171110.

(15) Albella, P.; Poyli, M. A.; Schmidt, M. K.; Maier, S. A.; Moreno, F.; Sáenz, J. J.; Aizpurua, J. Low-loss electric and magnetic field-enhanced spectroscopy with subwavelength silicon dimers. *J. Phys. Chem. C.* **2013**, *117*, 13573-13584.

(16) Zywietz, U.; Schmidt, M. K.; Evlyukhin, A. B.; Reinhardt, C.; Aizpurua, J.; Chichkov, B. N. Electromagnetic resonances of silicon nanoparticle dimers in the visible. *ACS Photonics* **2015**, *2*, 913-920.

(17) Shibanuma, T.; Grinblat, G.; Albella, P.; Maier, S. A. Efficient third harmonic generation from metal-dielectric hybrid nanoantennas. *Nano Lett.* **2017**, *17*, 2647-2651.

(18) Bohren, C. F.; Huffman, D. R. *Absorption and Scattering of Light by Small Particles*; Wiley: New York, 1983.

(19) Spinelli, P.; Verschuuren, M. A.; Polman. A. Broadband omnidirectional antireflection coating based on subwavelength surface Mie resonators. *Nat Commun.* **2012**, *3*, 692.

(20) Chong, k. E.; Staude, I.; James, A.; Dominguez, J.; Liu, S.; Campione, S.; Subramania, G. S.; Luk, T. S.; Decker, M.; Neshev, D. N.; Brener, I.; Kivshar, Y. S. Polarization-independent silicon metadevices for efficient optical wavefront control. *Nano Lett.* **2015**, *15*, 5369-5374.

(21) Wu, C.; Arju, N.; Kelp, G.; Fan, J. A.; Dominguez, J.; Gonzales, E.; Tutuc, E.; Brener,

I.; Shvets, G. Spectrally selective chiral silicon metasurfaces based on infrared fano resonances. *Nat Commun.* **2014**, *5*, 3892.

(22) Krasnok, A. E.; Simovski, C. R.; Belov, P. A.; Kivshar, Y. S. Superdirective dielectric nanoantennas. *Nanoscale* **2014**, *6*, 7354-7361.

(23) Albella, P.; Shibanuma, T.; Maier, S. A. Switchable directional scattering of electromagnetic radiation with subwavelength asymmetric silicon dimers. *Sci. Rep.* **2015**, *5*, 18322.

(24) Shibanuma, T.; Matsui, T.; Roschuk, T.; Wojcik, J.; Mascher, P.; Albella, P.; Maier, S. A. Experimental demonstration of tunable directional scattering of visible light from all-dielectric asymmetric dimers. *ACS Photonics* **2017**, *6*, 7915.

(25) Bakker, R. M.; Permyakov, D.; Yu, Y. F.; Markovich, D.; Paniagua-Domínguez, Ramón.; Gonzaga, L.; Samusev, A.; Kivshar, Y.; Luk'yanchuk, B.; Kuznetsov, A. I. Magnetic and electric hotspots with silicon nanodimers. *Nano Lett.* **2015**, *15*, 2137-2142.

(26) Boudarham, G.; Abdeddaim, R.; Bonod, N. Enhancing the magnetic field intensity with a dielectric gap antenna. *Appl. Phys. Lett.* **2014**, *104*, 021117.

(27) Taminiau, T. H.; Karaveli, S.; Karaveli, S.; van Hulst, N. F.; Zia, R. Quantifying the magnetic nature of light emission. *Nat Commun.* **2012**, *3*, 979.

(28) Craig, D. P.; Thirunamachandran, T. *Molecular Quantum Electrodynamics*; Academic Press: New York, 1984.

(29) Wu. T.; Zhang. X.; Wang, R.; Zhang. X. Strongly enhanced Raman optical activity in molecules by magnetic response of nanoparticles. *J. Phys. Chem. C* **2016**, *120*, 14795-14804.

(30) Imamoğlu, A. Cavity QED based on collective magnetic dipole coupling: spin ensembles as hybrid two-level systems. *Phys. Rev. Lett.* **2009**, *102*, 083602.

(31) Soykal, Ö. O.; Flatté, M. E. Strong field interactions between a nanomagnet and a photonic cavity. *Phys. Rev. Lett.* **2010**, *104*, 077202.

(32) Liu, M. P.; Li, C. H.; Du, H. B.; You, X. Z. Facile preparation of silicon hollow spheres and their use in electrochemical capacitive energy storage. *Chem. Commun.* **2012**, *48*, 4950-4952.

(33) Huang, X.; Yang, J.; Mao, S.; Chang, J.; Hallac, P. B.; Fell, C. R.; Metz, B.; Jiang, J.; Hurley. P. T.; Chen, J.; Controllable synthesis of hollow Si anode for long-cycle-life lithium-ion batteries. *Adv. Mater.* **2014**, *26*, 4326-4332.

(34) Mulholland, G. W.; Bohren, C. F.; Fuller, K. A. Light scattering by agglomerates: coupled electric and magnetic dipole method. *Langmuir* **1994**, *10*, 2533-2546.

(35) Borghese, F.; Denti, P.; Saija, R. *Scattering from Model Nonspherical Particles*; Springer: Berlin, 2007.

(36) Green, M. A.; Keevers, M. J. Optical properties of intrinsic silicon at 300 K. *Prog. Photovoltaics.* **1995**, *3*, 189-192.

(37) Rioux, D; Vallières, S.; Besner, S.; Muñoz, P.; Mazur, E.; Meunier, M. An analytic model for the dielectric function of Au, Ag, and their alloys. *Adv. Opt. Mater.* **2014**, *2*, 176-182.

(38) Johnson, P. B.; Christy, R. W. Optical constants of noble metals. *Phys. Rev. B* **1972**, *6*, 4370-4379.

(39) Hövel, H.; Fritz, S.; Hilger, A.; Kreibig, U. Width of cluster plasmon resonances: bulk dielectric functions and chemical interface damping. *Phys. Rev. B* **1993**, *48*, 18178-18188.

(40) Moroz, A. Electron mean free path in a spherical shell geometry. *J. Phys. Chem. C* **2008**, *112*, 10641-10652.

(41) Alonso-González, P.; Albella, P.; Schnell, M.; Chen, J.; Huth, F.; García-Etxarri, A.; Casanova, F.; Golmar, F.; Arzubiaga, L.; Hueso, L. E.; Aizpurua, J.; Hillenbrand, R. Resolving the electromagnetic mechanism of surface-enhanced light scattering at single hot spots. *Nat Commun.* **2012**, *3*, 684.

(42) Campione, S.; Guclu, C.; Ragan, R.; Capolino, F. Enhanced magnetic and electric fields via fano resonances in metasurfaces of circular clusters of plasmonic nanoparticles. *ACS Photonics* **2014**, *1*, 254-260.

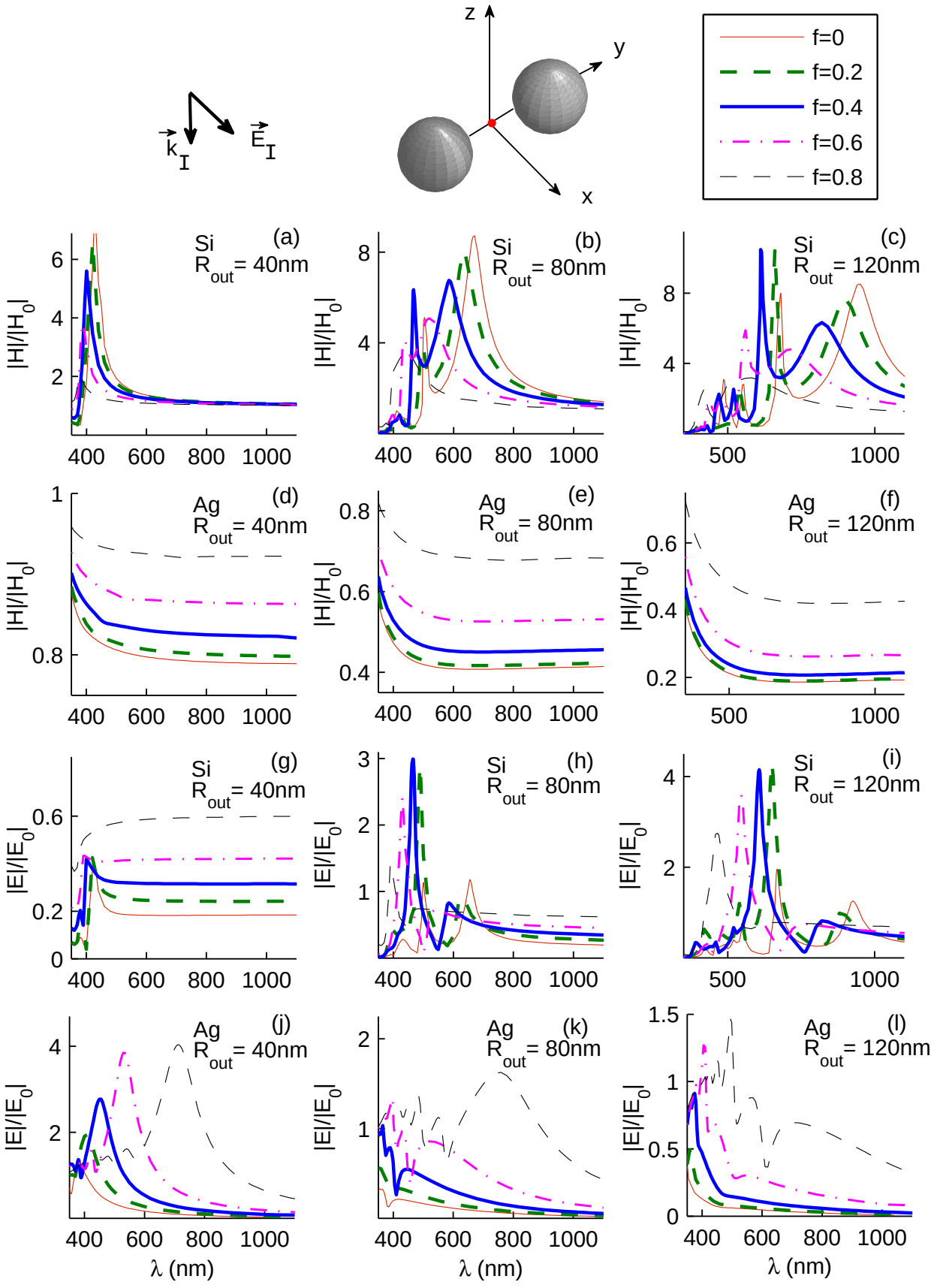

Figure 2: The field enhancement factors for Si dimers and Ag dimers. (a)-(f) $|H/H_0|$ and (g)-(l) $|E/E_0|$ as a function of the wavelength λ for various outer radii R_{out} and hollow sizes f. Here $\mathbf{E}_I \| \hat{\mathbf{x}}$, $\mathbf{k}_I = -k\hat{\mathbf{z}}$, and the fields are calculated at the dimer center $(\mathbf{r}_1 + \mathbf{r}_2)/2$.

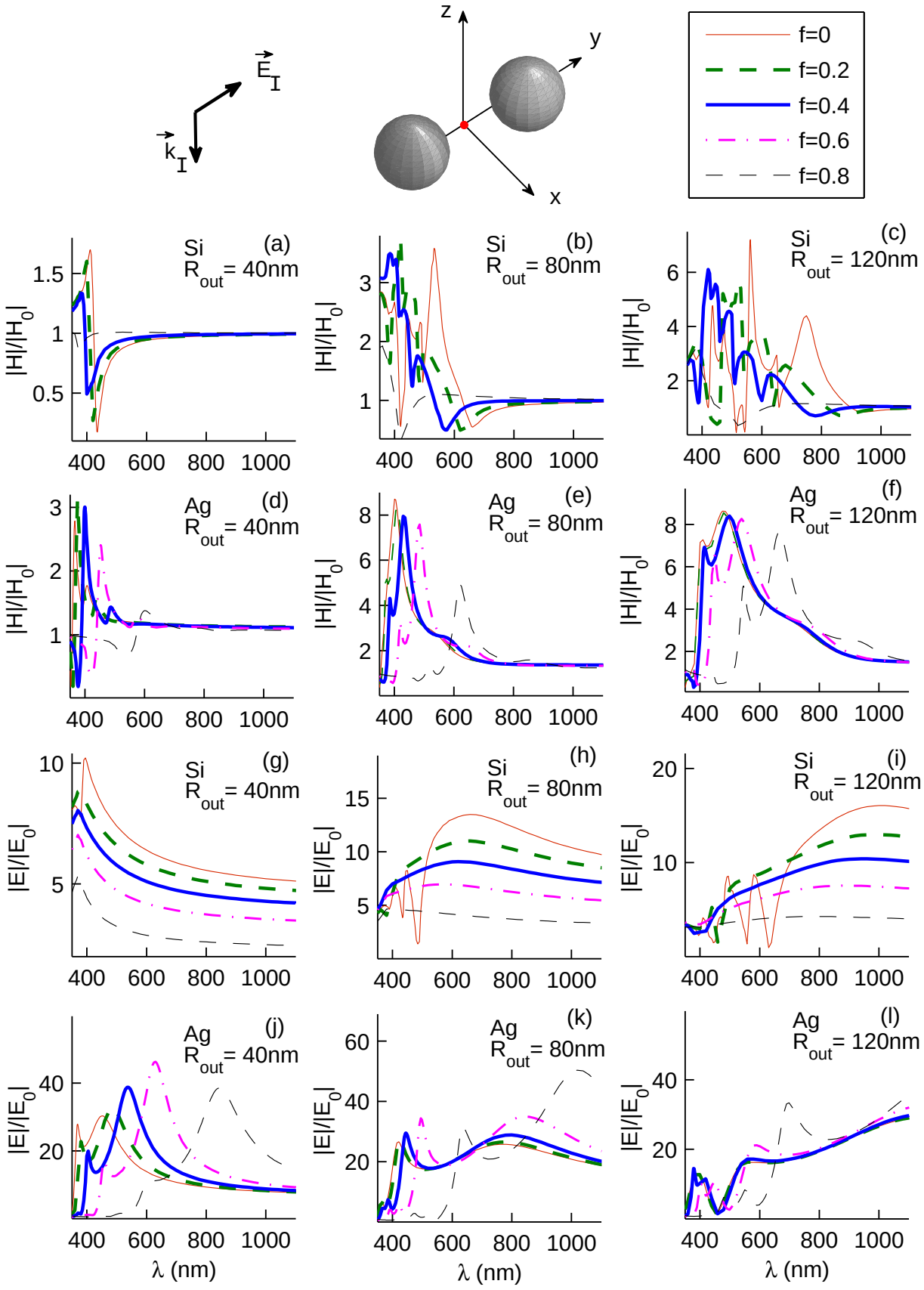

Figure 3: Same as Figure 2, but for $\mathbf{E}_I \parallel \hat{\mathbf{y}}$.

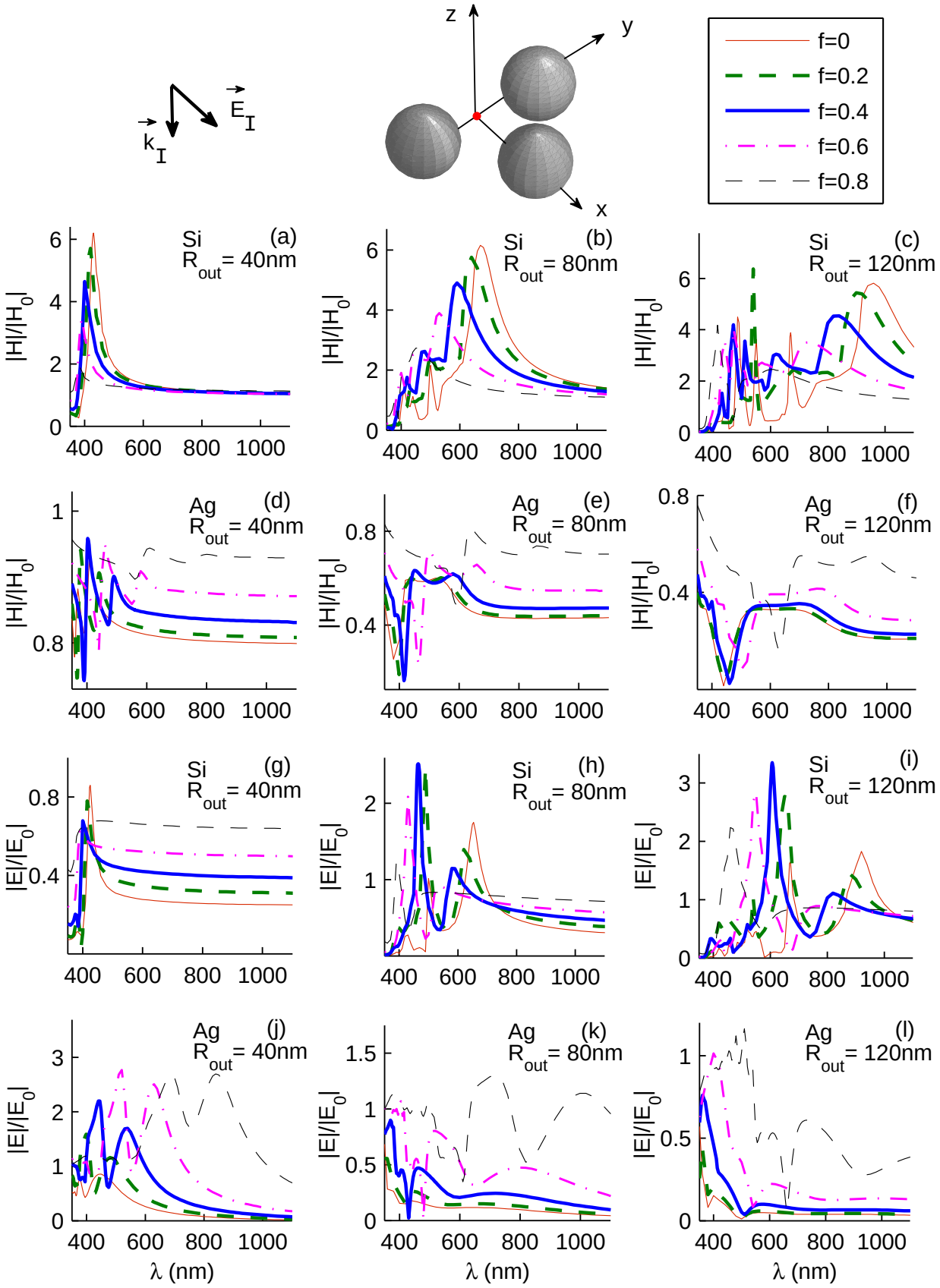

Figure 4: The field enhancement factors for Si trimers and Ag trimers. (a)-(f) $|H/H_0|$ and (g)-(l) $|E/E_0|$ as a function of the wavelength λ for various outer radii R_{out} and hollow sizes f. Here $\mathbf{E}_I \| \hat{\mathbf{x}}$, $\mathbf{k}_I = -k\hat{\mathbf{z}}$, and the fields are calculated at the midpoint $(\mathbf{r}_1 + \mathbf{r}_2)/2$.

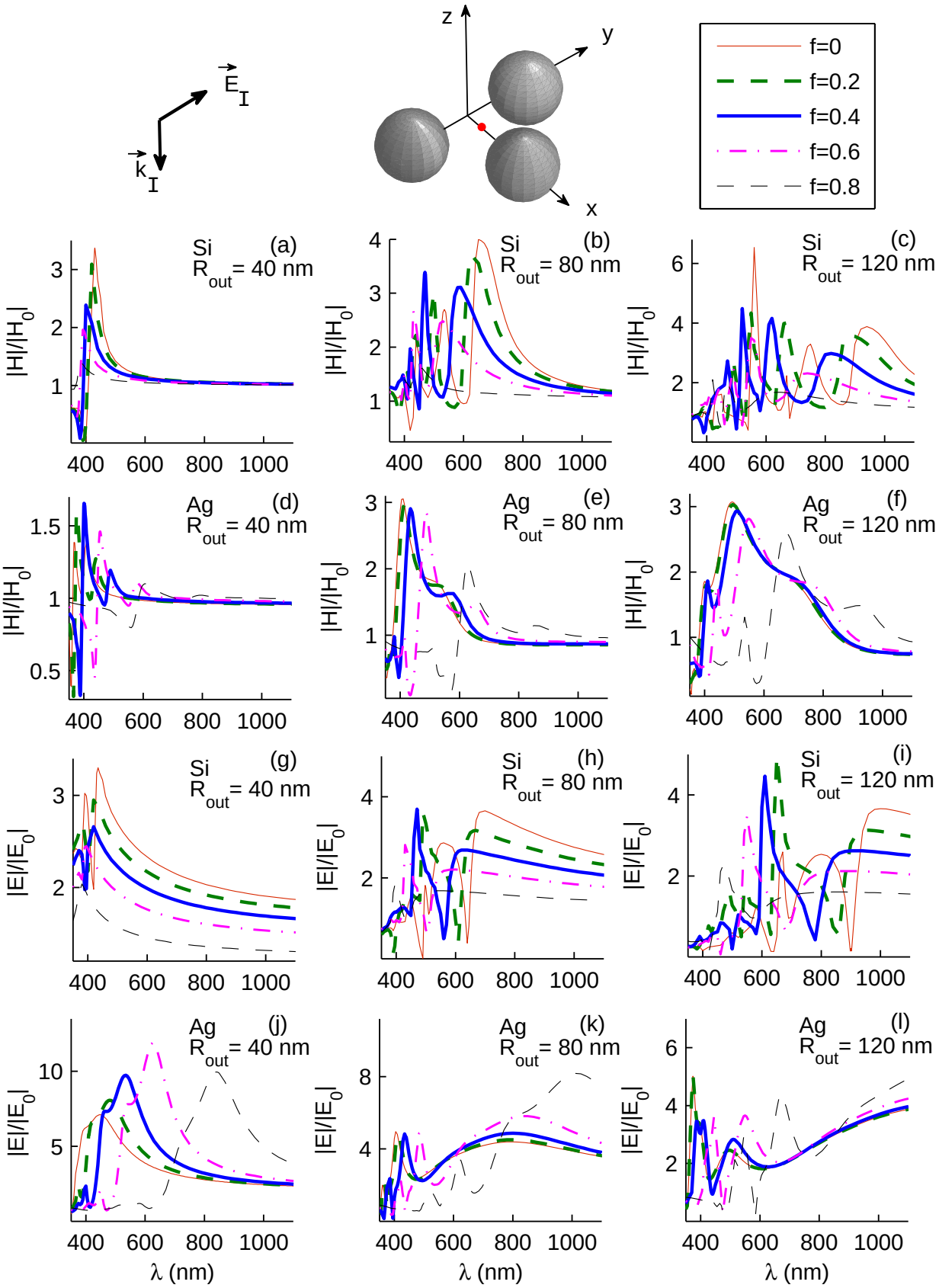

Figure 5: Same as Figure 4, but here the fields are calculated at the centroid $(\mathbf{r}_1+\mathbf{r}_2+\mathbf{r}_3)/3$. The enhancement factors are the same for both polarizations $\mathbf{E}_I \parallel \hat{\mathbf{x}}$ and $\mathbf{E}_I \parallel \hat{\mathbf{y}}$.

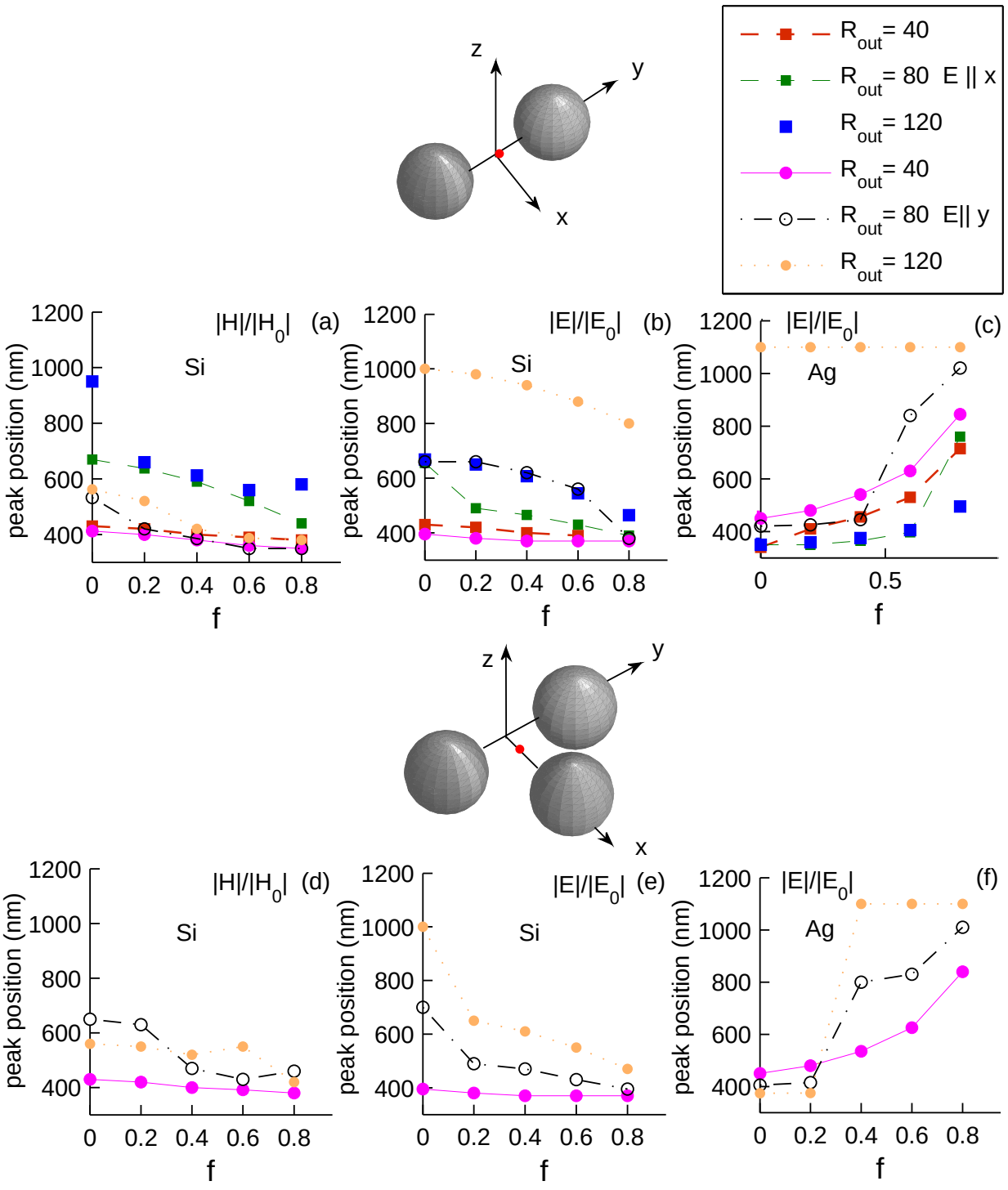

Figure 6: The position of the maximum (a) $|H/H_0|$ for a Si dimer, (b) $|E/E_0|$ for a Si dimer, (c) $|E/E_0|$ for a Ag dimer, (d) $|H/H_0|$ for a Si trimer, (e) $|E/E_0|$ for a Si trimer, and (f) $|E/E_0|$ for a Ag trimer, versus the hollow size f. The fields are calculated at the centroid of the cluster.

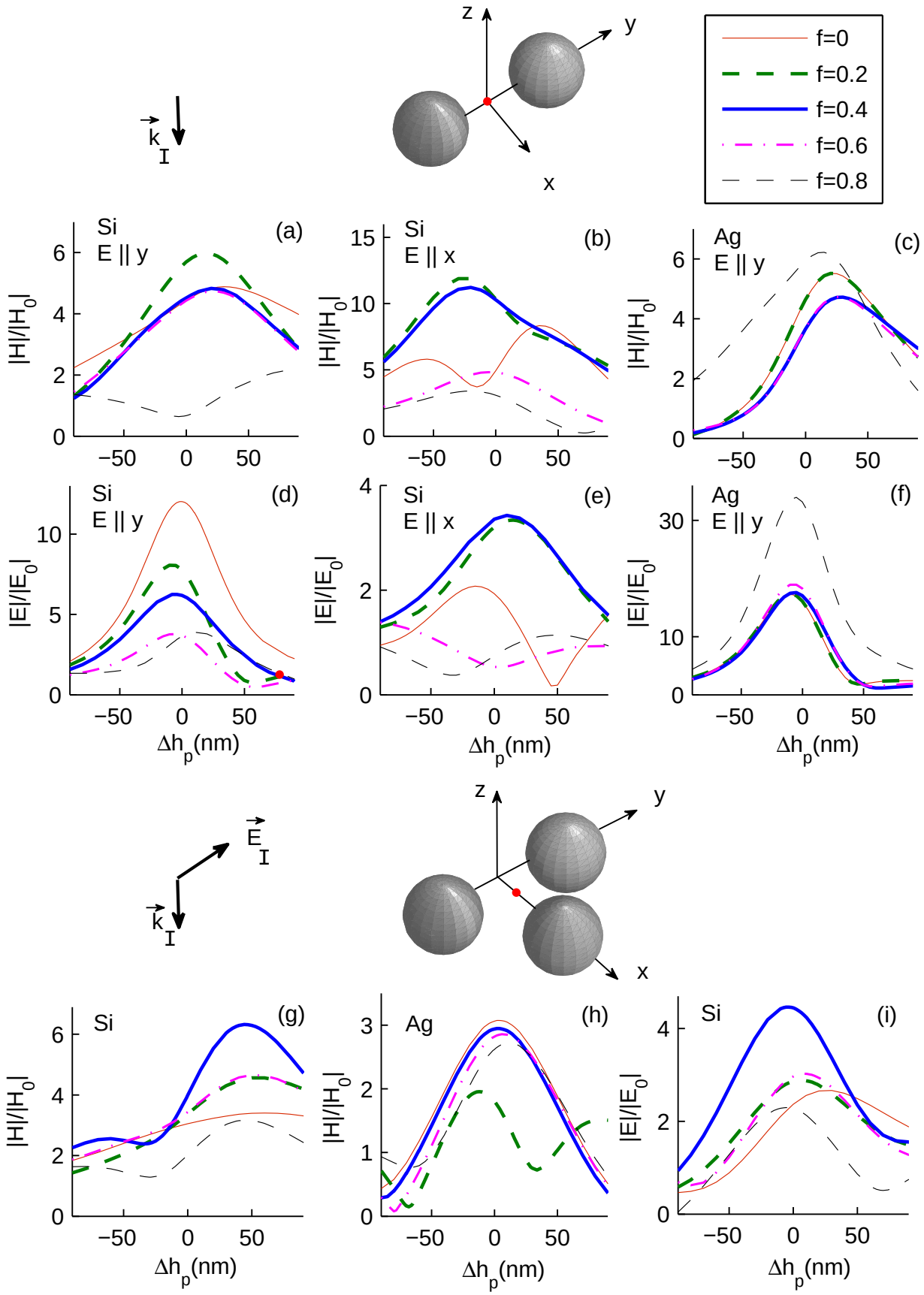

Figure 7: The field enhancement at the point $\mathbf{r}_c + \Delta h_p \hat{\mathbf{z}}$ as a function of Δh_p. When $f = (0, 0.2, 0.4, 0.6, 0.8)$ the wavelength in nm is (a) and (d) $(750, 520, 500, 420, 500)$, (b) and (e) $(670, 660, 615, 710, 550)$, (c) and (f) $(600, 600, 700, 700, 700)$, (g) and (i) $(760, 680, 610, 560, 470)$, and (h) $(500, 405, 510, 550, 670)$. Here $R_{out} = 120$ nm and $\mathbf{k}_I = -k\hat{\mathbf{z}}$.

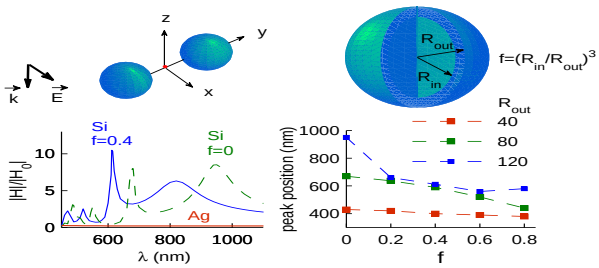

Figure 8: For Table of Contents Use Only.